Chemical Science

ROYAL SOCIETY OF CHEMISTRY

EDGE ARTICLE

View Article Online
View Journal

Cite this: DOI: 10.1039/d6sc01429a

All publication charges for this article have been paid for by the Royal Society of Chemistry

Stabilizing O3-type layered oxide cathodes *via* dual-site co-doping for long-life sodium–ion batteries

Xuejie Bai,[a] Qian Yang,[a] Yaning Wu,[a] Mingyue Li,[a] Genliang Yu,[a] Tongtong Huo,[a] Xiaobo Zhang,[a] Jie Xu,[a] Xunzhu Zhou,[b] Ting Lv,[a] Lin Li,[b]* Kaixiang Lei[a]* and Shijian Zheng*[a]

Received 18th February 2026
Accepted 27th May 2026

DOI: 10.1039/d6sc01429a

rsc.li/chemical-science

O3-type layered transition metal oxide cathode materials exhibit tremendous potential for commercial applications owing to their high theoretical capacity. However, their practical application is fundamentally limited by oxygen loss caused by irreversible oxygen redox reactions, as well as significant volume variation during Na^+ intercalation/deintercalation under high voltage conditions. To address these challenges, $Na_{0.98}Ca_{0.01}Ni_{0.33}Fe_{0.28}Ti_{0.05}Mn_{0.315}Sn_{0.015}O_2$ (CST-NFM) was designed and synthesized by co-doping with Sn^{4+}/Ti^{4+} in the transition metal layer and Ca^{2+} in the alkali metal layer. Dual-site doping modulates the band structure between TM and O through the synergistic effect of inert ions, effectively suppressing oxygen release, alleviating the severe volume fluctuations caused by irreversible phase transitions, and thereby enhancing the structural stability and cycling stability of the materials. As a result, the CST-NFM electrode exhibited a capacity retention of 72.69% after 500 cycles. Meanwhile, the corresponding full cell paired with hard carbon delivered an initial discharge specific capacity of 142.16 mAh g^{-1} and maintained a capacity retention of 86.37% after 200 cycles. This work demonstrates an effective and scalable approach for designing highly stable, high-performance layered oxide cathode materials for sodium–ion batteries through the synergistic effects of inert ion co-doping.

Introduction

Sodium–ion batteries (SIBs) have emerged as a promising alternative for large-scale energy storage due to their cost-effectiveness, enhanced safety, and rapid kinetics.[1–7] The cathode material governs the overall cycling stability and energy density of SIBs.[8–11] Among the discovered cathode materials, layered transition metal oxides (Na_xTMO_2) have garnered significant attention owing to their high specific capacity, considerable operating voltage, and mature synthesis process.[12–15] However, under deep desodiation conditions (>4.0 V *vs.* Na^+/Na), the energy level of the O 2p orbitals in O3-type cathode materials migrates toward the Fermi level, which compels the partial removal of their electrons and forces lattice oxygen to participate in redox reactions.[10,16] Although this process contributes additional specific capacity, it simultaneously induces irreversible lattice oxygen loss.[17] The extraction of lattice oxygen weakens the TM–O bonds, triggering transition metal dissolution and phase transformations from the layered structure to rock-salt or spinel phases.[10,18] These factors collectively lead to capacity fading, voltage decay, and even thermal runaway triggered by vigorous reactions between the evolved oxygen and the electrolyte.[19–21] Therefore, effectively suppressing oxygen loss at high voltages and enhancing structural stability are key to developing SIBs with high specific capacity and long-term cyclability.

To address the aforementioned bottlenecks, ion doping has emerged as a conventional yet straightforward and effective strategy, which involves introducing foreign ions to modulate lattice parameters, thereby enhancing the intrinsic stability of layered oxide cathode materials. According to the number of doping sites, the methods of ion doping are mainly classified into single-site doping,[22–26] dual-site doping[27–30] and multi-site doping.[31–33] These strategies fundamentally aim to modulate the coordination environment of transition metals and oxygen, thereby stabilizing the framework and enhancing the cycling lifespan of the material. Although the doping strategies described above have demonstrated certain efficacy in stabilizing the structure of layered oxide cathodes and improving their electrochemical performance, this comes at the cost of reduced capacity.[10] Moreover, the intrinsic correlation between ion doping and oxygen evolution remains inadequately investigated. Elucidating the intrinsic correlation between ion

[a]*Tianjin Key Laboratory of Materials Laminating Fabrication and Interface Control Technology, School of Materials Science and Engineering, Hebei University of Technology, Tianjin 300401, China. E-mail: kaixianglei@hebut.edu.cn; sjzheng@hebut.edu.cn*

[b]*College of Chemistry and Materials Engineering, Wenzhou University, Wenzhou, Zhejiang 325035, China. E-mail: linli@wzu.edu.cn*

doping and oxygen evolution is of decisive significance for overcoming the current performance bottlenecks of O3-type layered oxide cathode materials.

Herein, a stable layered oxide cathode material, $Na_{0.98}Ca_{0.01}Ni_{0.33}Fe_{0.28}Ti_{0.05}Mn_{0.315}Sn_{0.015}O_2$ (denoted as CST-NFM), was successfully fabricated through the strategic doping of Ca^{2+}, Sn^{4+}, and Ti^{4+} ions. Density functional theory (DFT) calculations indicate that the dopant ions modulate the band structure, shifting the distance from the O 2p p-band centre to the Fermi level from −2.645 eV to −2.667 eV, which makes electron extraction from oxygen more difficult. The difference between the d-band centre of Ni/Fe/Mn 3d orbitals and the p-band centre of O 2p orbitals decreases from 0.489 eV to 0.449 eV, indicating enhanced hybridization between the TM 3d and O 2p orbitals. In addition, the TM–O bond length shortens from 2.08 Å to 2.05 Å, and the covalency of the Ni–O, Fe–O, and Mn–O bonds increases. These results collectively improve the structural stability of the material. Meanwhile, Ca^{2+} doping in the sodium layer expands the interlayer spacing, which mitigates the volume variation caused by unfavourable phase transitions during cycling. *In situ* X-ray diffraction (XRD) and high-angle annular dark-field scanning transmission electron microscopy (HAADF-STEM) confirm the superior structural stability of CST-NFM. In addition, the CST-NFM cathode material effectively inhibits oxygen release and the dissolution of transition metals. Benefiting from these synergistic merits, the CST-NFM||HC full cell exhibits 86.37% capacity retention after 200 cycles, demonstrating exceptional cycling stability and considerable potential for practical applications. This work provides a valuable reference for the rational design of high-performance cathode materials for SIBs.

Results and discussion

O3-type layered oxide cathode materials suffer from transition metal dissolution, oxygen release, and irreversible phase transitions under high voltage, which severely restrict their practical applications.[34] Herein, a dual-site doping strategy is proposed to enable superior high-voltage stability by modulating the band structure between TM and O (Fig. 1a). The ionic radius of Ca^{2+} is close to that of Na^+ but significantly larger than that of typical transition metal ions, making it more favorable to occupy the Na sites. As an electrochemically inactive element, Ca^{2+} acts as a pillar to uphold the structure upon cycling. The enlarged interlayer spacing of the Na layers resulting from Ca^{2+} occupation accelerates Na^+ diffusion. Moreover, it can effectively shield the repulsive O–O interactions and suppress the sliding of transition metal layers, thus alleviating the detrimental phase transitions. High-valent Sn^{4+}($[Kr]4d^{10}$) and Ti^{4+}($[Ar]3d^0$) tend to occupy TM sites. Their distinct electronic configurations can increase the electron cloud density around oxygen, indirectly enhancing the bonding strength between transition metals and oxygen. This in turn suppresses the lattice oxygen redox reaction and improves the structural stability of the material. Density functional theory (DFT) calculations were performed to investigate the effect of element doping on the electronic

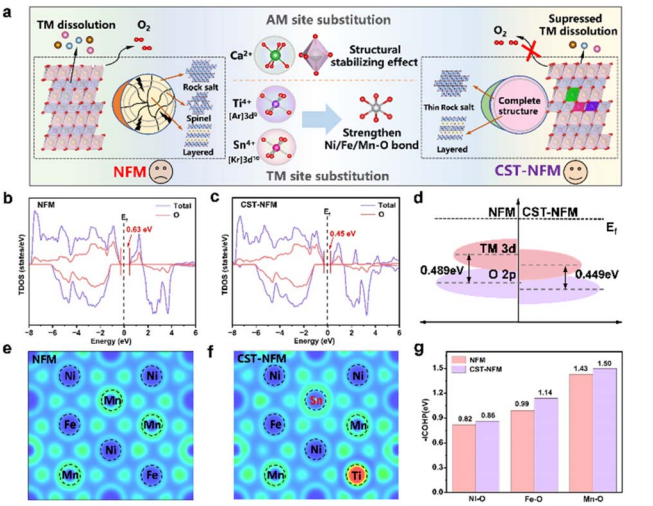

Fig. 1 (a) Schematic illustration of the failure mechanism of NFM and the improvement mechanism of CST-NFM. Total density of states of (b) NFM and (c) CST-NFM. (d) The band structure diagram. The interfacial diagram of the electron density of the TMO_6 layers along the [001] direction in (e) NFM and (f) CST-NFM. (g) −ICOHP of Ni–O, Fe–O, and Mn–O bonds in NFM and CST-NFM.

structure, and the corresponding optimized geometries are shown in Fig. S1.

As shown in Fig. 1b and c, CST-NFM exhibits a narrower band gap (0.45 eV) compared with NFM (0.63 eV), indicating enhanced electronic conductivity favourable for charge diffusion.[35–37] The projected density of states (PDOS) revealed that Ca^{2+}, Sn^{4+} and Ti^{4+} exhibit almost no orbital hybridization with oxygen, which facilitates the redistribution of electrons (Fig. S2).[32,38,39] Furthermore, the calculated p-band centre energies for O 2p in NFM and CST-NFM are −2.645 eV and −2.667 eV, respectively. The p-band centre of O 2p in CST-NFM is farther from the Fermi level, indicating that electron extraction from oxygen is more challenging in the deeply desodiated state. This finding demonstrates that oxygen redox reactions are less prone to occur.[37] It is noteworthy that the d-band centres of the Ni/Fe/Mn 3d orbitals in NFM and CST-NFM cathodes are located at −2.156 eV and −2.218 eV, respectively. The energy differences between these d-band centres and the O 2p p-band centres are 0.489 eV and 0.449 eV, as illustrated in the energy level diagram in Fig. 1d. Compared with NFM, the smaller d–p band centre separation in CST-NFM indicates stronger Ni/Fe/Mn–O orbital hybridization, which in turn enhances structural stability.[40]

The electron localization function (ELF) in the [001] direction of the transition metal and oxygen is illustrated for NFM and CST-NFM. The incorporation of Sn^{4+} and Ti^{4+} reconstructs the local electronic structure, which enhances electron localization around oxygen in Fig. 1e, f and S3. Consequently, this mitigates the extraction of electron density from oxygen during deep desodiation and improves structural stability.[41–43] Crystal orbital Hamilton population (COHP) calculations were performed to evaluate the strength of TM–O covalent bonds. As shown in Fig. 1g and S4, the larger –ICOHP values for Ni–O, Fe–

O, and Mn–O bonds in CST-NFM indicate stronger covalent character compared to NFM, demonstrating enhanced structural stability of the doped material.[44,45] These results indicate that Ca^{2+}, Sn^{4+}, and Ti^{4+} do not hybridize with oxygen, which shifts the O 2p p-band centre away from the Fermi level. Such electronic modulation optimizes the intrinsic electronic structure, strengthens the strength of Ni–O, Fe–O, and Mn–O covalent bonds, mitigates oxygen loss, and thereby improves the structural stability simultaneously.

NFM ($NaNi_{0.33}Fe_{0.33}Mn_{0.33}O_2$) and CST-NFM ($Na_{0.98}Ca_{0.01}Ni_{0.33}Fe_{0.28}Ti_{0.05}Mn_{0.315}Sn_{0.015}O_2$) were synthesized *via* a facile high-temperature solid–state reaction. The stoichiometric ratios of these layered oxide cathodes were quantified using inductively coupled plasma optical emission spectroscopy (ICP-OES) (Table S1), consistent with the experimental design. To investigate the effect of doping on the crystal structure, XRD testing was first conducted. The results showed that the diffraction patterns of both NFM and CST-NFM exhibited high agreement with the standard O3-type layered oxide pattern (PDF #54-0887), belonging to the hexagonal crystal system with the space group $R\bar{3}m$. This confirms the successful synthesis of the materials. Weak NiO diffraction peaks were observed in the ranges of 37°–40° and 43°–45°, attributed to the solubility limit of nickel in the O3-type lattice.[46] The co-doping of $Ca^{2+}/Sn^{4+}/Ti^{4+}$ induces a low-angle shift of the (003) peak (2θ = 15.5°–17.5°), which corresponds to an increased *c*-axis lattice parameter (Fig. S5).[40] Subsequently, detailed structural information for NFM and CST-NFM was obtained *via* Rietveld refinement of the XRD patterns (Fig. 2a, b and Tables S2–4). Rietveld analysis confirms the successful doping and site occupancy: Sn^{4+} and Ti^{4+} are located at the octahedral 3b Wyckoff sites in the TM layer, and Ca^{2+} is situated at the octahedral 3a Wyckoff sites in the AM layer. As shown in Fig. 2c and d, the Rietveld refinement results reveal that the elongation of Na–O bonds expands the sodium layers, thereby providing more spacious migration pathways for Na^+ ions and thus optimizing their diffusion kinetics. Conversely, the shortening of TM–O bonds contracts the transition-metal layers, which strengthens interlayer interactions and consequently enhances structural stability.[47]

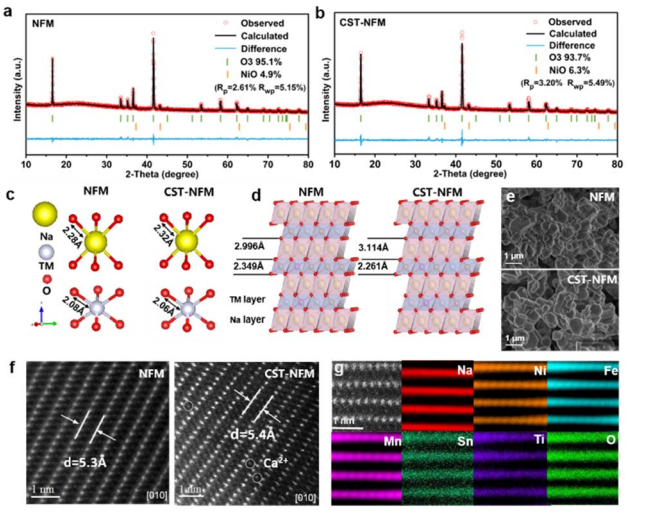

Fig. 2 Rietveld refinement patterns of the XRD data for (a) NFM and (b) CST-NFM. (c) Changes in Na–O and TM–O bond lengths obtained from Rietveld refinement. (d) Schematic diagrams of the crystal structures of NFM and CST-NFM. (e) SEM images of NFM and CST-NFM. (f) HAADF-STEM images of NFM and CST-NFM from [010] zone-axes. (g) HAADF-STEM image and atomic-scale EDS mapping of CST-NFM.

Scanning electron microscopy (SEM) and transmission electron microscopy (TEM) were employed to characterize the morphology and microstructure of both NFM and CST-NFM. Both materials exhibit bulk-like particles with diameters of approximately 1 μm, indicating that the dopant elements have a negligible influence on the overall morphology (Fig. 2e). TEM images reveal clear lattice fringes in both NFM and CST-NFM samples, corresponding to the [003] plane of the O3-phase structure, as illustrated in Fig. S6. The increased *d*-spacing of the [003] plane in CST-NFM (5.4 Å *vs.* 5.3 Å in NFM) facilitates Na^+ diffusion, which is in full agreement with the lattice parameters obtained from XRD Rietveld refinement. Furthermore, energy-dispersive X-ray spectroscopy (EDS) elemental mapping confirms the homogeneous distribution of constituent elements in both NFM and CST-NFM (Fig. S7 and 8). The influence of doping on the valence states of transition metals (TMs) was investigated using X-ray absorption near-edge structure (XANES) spectroscopy at the TM K-edges. The Ni, Fe, and Mn K-edge XANES spectra of both NFM and CST-NFM exhibit negligible shifts, indicating no significant change in valence states after doping (Fig. S9).[29,48]

Subsequently, the atomic-scale structural features of the pristine NFM and CST-NFM cathodes were investigated using aberration-corrected scanning transmission electron microscopy (STEM) in high-angle annular dark-field (HAADF) mode. The obtained image clearly reveals the characteristic bright-dark contrast between the transition metal (TM) and alkali metal (AM) layers (Fig. 2f). The appearance of intermittent bright spots in the AM layer of CST-NFM provides direct atomic-scale evidence for the substitutional doping of Ca^{2+} into sodium sites.[27,29] The atomic-scale EDS elemental mapping for Na, Ca, Ni, Fe, Mn, Ti, Sn, and O elements in CST-NFM is applied to reveal the atomic occupancy sites. As shown in Fig. 2g and S10, the Ni, Fe, Mn, Ti, and Sn ions occupy the TM layer. Owing to the low doping concentration and relatively light atomic mass of Ca^{2+} ions, faint lattice stripes corresponding to Ca^{2+} ions occupying the Na layer can be discerned in the atomic-scale EDS elemental mapping.

To gain deeper insights into the electrochemical reaction mechanisms of NFM and CST-NFM electrodes during charge/discharge processes, cyclic voltammetry (CV) measurements were performed on half-cells at a scan rate of 0.1 mV s^{-1} within a voltage range of 2.0–4.2 V. A smaller potential difference (ΔV) between the redox peaks in the CV curves correlates with a lower polarization and higher electrochemical reversibility of the electrode reaction. As shown in Fig. 3a, the reduced ΔV value in CST-NFM demonstrates its lower polarization and enhanced cycling reversibility. In Fig. 3b, the initial discharge specific capacities of CST-NFM and NFM cathodes are 148.74 mAh g^{-1} and 156.83 mAh g^{-1}, respectively. This indicates that the

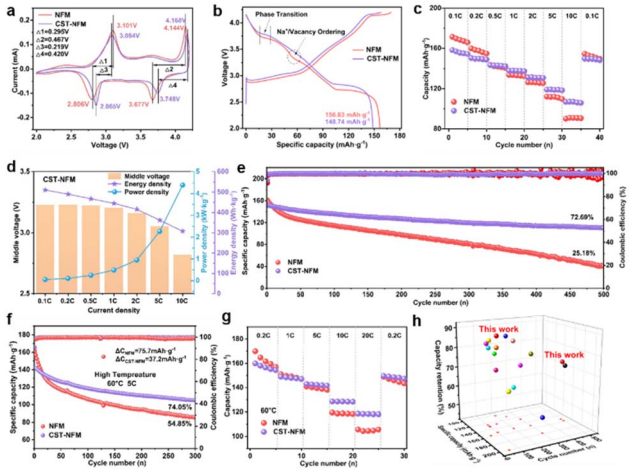

Fig. 3 (a) CV curves of NFM and CST-NFM for the first cycle at 0.1 mV s^{-1}. (b) Initial charge–discharge curves of NFM and CST-NFM at 1C. (c) Rate performance of NFM and CST-NFM. (d) Median voltage, energy density and power density of CST-NFM at different current densities. (e) Long-term cycling performance at 1.0C. (f) Cycling performance and (g) rate performance at a high temperature of 60 °C. (h) Comparison of cycling performance with the reported literature.

incorporation of inert ions does not significantly sacrifice capacity. The discharge plateau at 3.82 V for CST-NFM and 3.79 V for NFM corresponds to the occurrence of phase transitions. The difference between the two discharge plateaus arises because the doping of inert ions suppresses irreversible phase transitions during cycling, thereby helping to improve the cycling stability of the material.[49] The difference in the discharge plateau at around 3.3 V is attributed to the suppression of Na^+/vacancy ordering by the introduction of three inert ions, which facilitates Na^+ transport.[27,50,51] As shown in Fig. 3c and S11, the reversible capacities of the CST-NFM cathode at 0.1C, 0.2C, 0.5C, 1.0C, 2.0C, 5.0C, and 10.0C are 158.13, 150.16, 143.52, 137.96, 131.28, 119.14, and 106.83 mAh g^{-1}, respectively. The improved rate capability can be attributed to the expansion of the Na layer spacing induced by Ca^{2+}, Sn^{4+}, and Ti^{4+} doping, which broadens the diffusion channels for Na^+ migration. Concurrently, this structural optimization endows CST-NFM with a higher average working voltage, energy density, and power density, as illustrated in Fig. 3d and S12. In addition, dual-site doping exhibits superior cycling stability compared to single-site doping, demonstrating the synergistic effect of co-doping with inert ions (Fig. S13).[38] CST-NFM achieves a capacity retention of 72.69% after 500 cycles at 1.0C, far exceeding that of NFM (25.18%), as depicted in Fig. 3e. After 500 cycles, the NFM electrode exhibited significant charge–discharge voltage hysteresis, indicating a marked increase in polarization during cycling. In contrast, the CST-NFM electrode demonstrated well-overlapping charge–discharge curves with minimal voltage decay, suggesting maintained structural stability throughout the cycling process. (Fig. S14 and 15). Subsequently, we investigated the influence of different areal loadings of the cathode electrodes for both materials on their electrochemical performance to evaluate their practical viability. As shown in Fig. S16, CST-NFM exhibits significantly better capacity retention than NFM after 100 cycles under areal loadings of 1, 3, and 5 mg cm^{-2}. Furthermore, we also conducted high-temperature performance tests on both NFM and CST-NFM materials (Fig. 3f and S17). When the operating temperature was raised to 60 °C, the CST-NFM material exhibited a capacity retention rate of 74.05% after 300 cycles, demonstrating a significantly higher capacity retention compared to NFM (54.85%). Moreover, CST-NFM also exhibited outstanding rate capability at 60 °C (118.59 mAh g^{-1} at 20.0C) as shown in Fig. 3g and S18. The rate performance at elevated temperature is superior to that at room temperature because the higher temperature promotes Na^+ diffusion within the bulk material and accelerates charge transfer kinetics at the electrode/electrolyte interface.[52] Compared with NFM, the optimized CST-NFM exhibits a greater improvement in electrochemical performance, which is attributed to the dual-site co-doping strategy that suppresses the dissolution of transition metal ions and inhibits the electrode/electrolyte interfacial side reactions at 60 °C (Fig. S19). Compared with previously reported studies, the CST-NFM cathode demonstrates pronounced advantages in electrochemical performance (Fig. 3h).[15,22,25,36,40,41,53–60]

CV measurements at various scan rates (0.1, 0.2, 0.4, 0.6, 0.8, and 1.0 mV s^{-1}) within 2.0–4.2 V were performed to study the Na^+ diffusion kinetics, as shown in Fig. S20. The results reveal that CST-NFM exhibits superior cycling reversibility and lower polarization compared to NFM. The quantitative analysis of the I_p and $v^{1/2}$ plot reveals a linear correlation. This process is guided by ion diffusion. The markedly higher slope of CST-NFM compared to NFM confirms improved Na^+ transport kinetics due to doping.[61] Galvanostatic intermittent titration technique (GITT) measurements observed a higher Na^+ diffusion coefficient in CST-NFM compared to NFM, demonstrating that the dopant elements enhance the Na^+ diffusion kinetics, as shown in Fig. S21. To further probe the kinetic evolution during cycling, electrochemical impedance spectroscopy (EIS) was performed before cycling and after different cycle numbers (Fig. S22). The results show that CST-NFM exhibits lower impedance values than NFM, indicating a more stable interface structure and faster charge-transfer kinetics in the CST-NFM electrode. In summary, the modified crystal structure through doping facilitates Na^+ transport by providing broader diffusion channels and simultaneously promotes electron transfer *via* reduced activation energy, leading to markedly improved Na^+ diffusion kinetics in CST-NFM.

The influence of dopants on the structural evolution of the cathodes during cycling was investigated by *in situ* XRD measurements (Fig. 4a, b and S23–24). During charging, the extraction of Na^+ and oxidation of transition metal ions shift the (003) and (006) diffraction peaks toward lower angles, indicating expansion along the *c*-axis. This interlayer expansion results from enhanced electrostatic repulsion between adjacent oxygen layers after Na^+ removal.[27] The (101), (012), and (104) diffraction peaks shift toward higher angles, indicating contraction within the ab plane. Subsequently, the (003) and (104) peaks rapidly weaken and vanish, accompanied by the

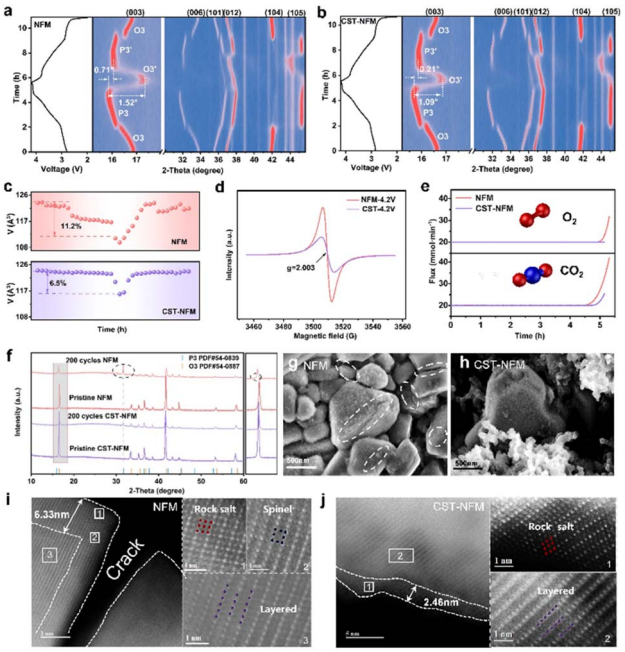

Fig. 4 Contour maps of *in situ* XRD of (a) NFM and (b) CST-NFM. (c) Volume changes of NFM and CST-NFM. (d) EPR spectra of NFM and CST-NFM at 4.2 V-charged state. (e) *In situ* DEMS results of NFM and CST-NFM during the first charge to 4.2 V. (f) XRD spectra of pristine NFM and CST-NFM cathodes and those after 200 cycles at 1.0C. SEM images of (g) NFM and (h) CST-NFM after 200 cycles. HAADF-STEM images of (i) NFM and (j) CST-NFM after 200 cycles at 3.0C during 2.0–4.2 V.

emergence of a P3(003) peak, indicating a phase transition from O3 to P3. When the voltage increases to 4.0 V, the P3 phase disappears, and only the (003) peak subsequently shifts toward higher angles. This peak should be assigned to the monoclinic O3′ phase (space group *C*2/*m*), which persists up to 4.2 V. During the subsequent discharge, the O3′ phase transforms into the monoclinic P3′ phase, which is associated with a discharge plateau at roughly 3.7 V. It finally reverts to the original O3 phase. The *in situ* XRD data (Fig. S25) demonstrate that both materials follow an asymmetric phase-transition pathway (O3 → P3 → O3′ → P3′ → O3) during cycling.[25,62] Notably, during the P3–O3′ transition, CST-NFM exhibits a smaller peak shift (1.09°) compared to NFM (1.52°). Moreover, across the P3 → O3′ → P3′ sequence, the net peak displacement is significantly reduced in CST-NFM (0.21°) relative to NFM (0.71°). These results indicate that the modified material possesses enhanced structural reversibility. The evolution of lattice parameters and cell volume during cycling was quantified through Rietveld refinement of the *in situ* XRD data for NFM and CST-NFM (Fig. 4c). Compared to NFM (11.2%), CST-NFM exhibits a significantly reduced volume change of 6.5% during cycling, accompanied by smaller fluctuations along the *a*- and *c*-axes (Fig. S26 and 27).

Oxygen vacancies in the NFM and CST-NFM samples were subsequently examined by electron paramagnetic resonance (EPR) spectroscopy. The concentration of oxygen vacancies correlates with the redox activity of oxygen and the release of oxygen. No pronounced EPR signal was detected in the initial electrodes (Fig. S28). Upon charging to 4.2 V, distinct signals corresponding to oxygen vacancies were observed at $g = 2.003$ for both materials in Fig. 4d. However, the signal intensity for NFM was significantly higher than that for CST-NFM. *In situ* differential electrochemical mass spectrometry (DEMS) was employed to monitor gas evolution during the first charge cycle of NFM and CST-NFM. As shown in Fig. 4e, CO_2 evolution is detected during charging for both materials, with CST-NFM exhibiting significantly less CO_2 release. This indicates that the decomposition of the electrolyte is effectively suppressed at high voltages.[47] Notably, O_2 evolution is observed in NFM upon charging to high voltage, which can lead to rapid capacity decay and structural collapse. In contrast, no O_2 release is detected throughout the entire charging process for CST-NFM, confirming the effective suppression of oxygen release by Ca^{2+}, Sn^{4+}, and Ti^{4+} co-doping. In addition, ICP-OES results indicate that the dissolution of Ni, Fe, and Mn in CST-NFM is significantly lower than that in NFM, demonstrating that the doping of Ca^{2+}, Sn^{4+}, and Ti^{4+} effectively suppresses the dissolution of transition metal ions (Fig. S29).

To further investigate the effect of Ca^{2+}, Sn^{4+}, and Ti^{4+} doping on the structural stability and particle integrity after prolonged cycling, XRD, SEM, TEM and HAADF-STEM characterizations were performed on both materials after 200 electrochemical cycles. As shown in Fig. 4f, after 200 cycles, characteristic peaks of the P3 phase emerge in the NFM cathode, indicating an irreversible O3–P3 phase transformation.[63] In contrast, CST-NFM maintains the pristine O3-type structure without phase change. The SEM and TEM micrographs demonstrate superior particle integrity for CST-NFM, in contrast to the evident crack formation on the surface of NFM (Fig. 4g, h and S30). The atomic-scale evolution was further probed *via* HAADF-STEM imaging using a spherical aberration-corrected microscope. As shown in Fig. 4i and S31, distinct surface cracks are observed on NFM after 200 cycles, which can be attributed to the accumulation of mechanical stress during prolonged cycling. Furthermore, prolonged cycling induces degradation of the layered structure, leading to an irreversible phase transformation characterized by a mixture of layered, spinel, and rock-salt phases.[30,64] This multiphase evolution obstructs Na^+ migration and consequently deteriorates electrochemical performance. By comparison, CST-NFM shows neither microcracks nor spinel-phase formation, preserving a layered bulk capped by a nanoscale rock-salt surface layer (Fig. 4j). This distinct structural evolution underscores the role of doping in preventing irreversible phase changes and ensuring structural robustness upon cycling (Fig. S32). In summary, Ca^{2+}, Sn^{4+}, and Ti^{4+} co-doping inhibits cyclic lattice distortion, alleviates mechanical stress, and curbs microcracking and TM dissolution, leading to markedly improved structural robustness.

To probe the charge compensation behavior, *ex situ* XPS analysis was conducted on NFM and CST-NFM electrodes at different states of charge. The reversible shifts of Ni 2p and Fe 2p peaks in the XPS spectra of CST-NFM between 4.2 V (charged) and 2.0 V (discharged) (Fig. 5a and b) demonstrate the active

participation of Ni and Fe in redox reactions for charge balance. In contrast, no appreciable binding-energy shifts are observed for the Mn 2p, Sn 3d, Ca 2p, and Ti 2p core-level spectra, indicating that these elements do not participate in charge compensation (Fig. S33). Likewise, Ni and Fe in NFM participate in charge compensation through reversible redox processes (Fig. S34). Notably, when charged to 4.2 V, CST-NFM exhibits a higher Ni^{4+}/Ni^{3+} ratio, with an average oxidation state reaching +3.62.[63] This indicates that CST-NFM possesses a higher oxidation state and excellent charge storage capability.[40] Meanwhile, CST-NFM shows a lower Fe^{4+}/Fe^{3+} ratio, suggesting that dual-site ion doping effectively suppresses the formation of Fe^{4+}, thereby inhibiting the Jahn–Teller effect.[48] Additionally, the electrochemical activity of lattice oxygen (O^{2-}) was investigated, as shown in Fig. 5c and S35. When fully charged to 4.2 V, a new functional group peak appears at 530.4 eV, attributed to (O_2^{n-}) species. Notably, the signal intensity of (O_2^{n-}) in CST-NFM is considerably lower than that in NFM, and after discharging to 2.0 V, the relative intensity of lattice oxygen in CST-NFM remains well preserved.[38,65] These results indicate that the doping of Ca^{2+}, Sn^{4+}, and Ti^{4+} suppresses the oxygen redox reaction and effectively inhibits oxygen loss.

In order to further monitor their valence state variations during the sodiation/desodiation process, Ni, Fe, and Mn K-edge XANES measurements were performed on NFM and CST-NFM. During charging, a pronounced shift in the Ni K-edge spectra of both NFM and CST-NFM is observed at 3.3 V, indicating the oxidation of $Ni^{2+} \rightarrow Ni^{3+}$. Upon further charging to 4.2 V, the Ni K-edge continues to shift toward higher energy, corresponding to the $Ni^{3+} \rightarrow Ni^{4+}$ oxidation, while the Fe K-edge also shifts to higher energy, signifying the oxidation of $Fe^{3+} \rightarrow Fe^{4+}$ (Fig. 5d, e and S36). The negligible shift in the Mn K-edge spectra for both samples is attributed to subtle alterations in the coordination geometry, not to valence variation, confirming the inert role of Mn during redox processes (Fig. 5f and S36).[66] The observed contraction of Ni/Fe–O and Ni/Fe–TM bond lengths in FT-EXAFS spectra during charging validates the active role of Ni and Fe in redox-based charge compensation (Fig. 5g, h and S37). The negligible change in the Mn–O bond length confirms that Mn remains electrochemically inert in Fig. 5i and S37. The above electrochemical tests indicate that both NFM and CST-NFM exhibit Ni and Fe as their electrochemically active elements, while the other inert elements act as structural pillars.[54]

Air stability stands as a paramount determinant for the scalable deployment of materials in commercial settings. The calcined materials were exposed to ambient air with approximately 70% relative humidity, and the impact of air exposure on their phase structures was first investigated *via* XRD. After 7 days of exposure to air, the O3 (003) diffraction peak of NFM exhibited a significant shift (0.20°) compared to that of CST-NFM (0.12°) in Fig. 6a and b. Simultaneously, as shown in Fig. 6c and d, the air-exposed CST-NFM cathode exhibited reduced capacity decay. After exposure to air for 4 days, CST-NFM still retains 85.09% of its capacity after 300 cycles, demonstrating its excellent air stability. Subsequently, full cells were assembled with hard carbon (HC) anode to evaluate the practical application potential of the CST-NFM cathode (Fig. 6e and S38). The CST-NFM‖HC full cell exhibits a high initial Coulombic efficiency of 93.30% and delivers a reversible specific capacity of 142.16 mAh g^{-1} (based on the cathode active mass) within a voltage window of 1.0–4.1 V. Notably, the CST-NFM‖HC full cell demonstrates outstanding cycling stability, retaining 86.37% of its initial capacity after 200 cycles. The above results confirm that CST-NFM exhibits excellent air stability and holds promising application potential in sodium–

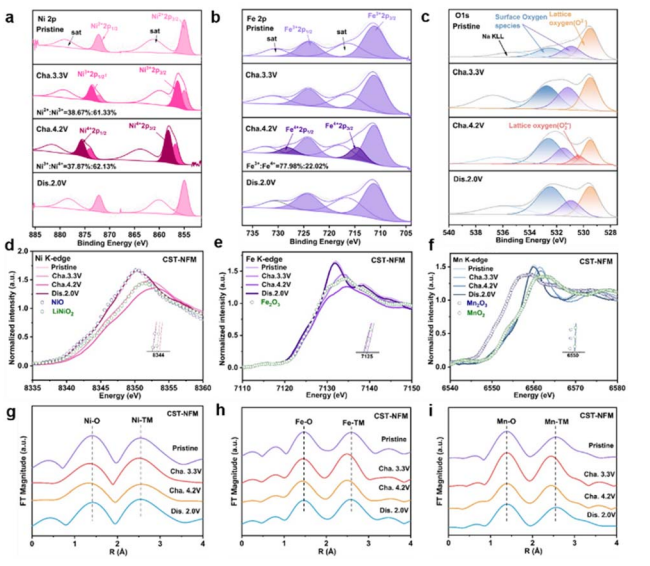

Fig. 5 XPS spectra of (a) Ni 2p, (b) Fe 2p, and (c) O 1s of CST-NFM. (d) Ni K-edge, (e) Fe K-edge, and (f) Mn K-edge XANES spectra of CST-NFM. (g) Ni K-edge, (h) Fe K-edge, and (i) Mn K-edge FT-EXAFS spectra of CST-NFM.

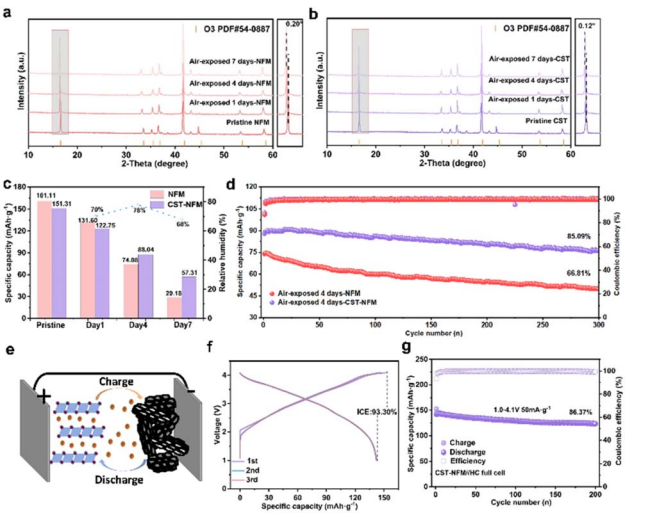

Fig. 6 XRD patterns of (a) NFM and (b) CST-NFM before and after air exposure. A comparison of the (c) specific capacity and (d) cycling performance of NFM and CST-NFM after air exposure. (e) Schematic diagram of the CST-NFM‖HC full cell. (f) Charge/discharge curves and (g) cycling performance of the CST-NFM‖HC full cell at 50 mA g^{-1}.

ion full cells, with its outstanding cyclability offering a reliable material platform for advanced sodium–ion storage systems.

Conclusions

In summary, a dual-site co-doping strategy was proposed and implemented, where Sn^{4+} and Ti^{4+} were introduced into the transition metal layer, and Ca^{2+} was doped into the alkali metal layer, resulting in the successful synthesis of a modified cathode material, $Na_{0.98}Ca_{0.01}Ni_{0.33}Fe_{0.28}Ti_{0.05}Mn_{0.315}Sn_{0.015}O_2$ (CST-NFM). The dual-site doping strategy modulates the band structure between TM and O, effectively suppressing the oxygen redox reaction under deep desodiation conditions, thereby enhancing the structural stability and cycling stability of the material. Specifically, this doping strategy effectively downshifts the energy level of the O 2p band centre away from the Fermi level, which fundamentally suppresses the excessive oxygen redox activity and effectively inhibits O_2 evolution during high-voltage charging processes. Meanwhile, the co-doping of inert ions significantly alleviates the volume fluctuation of the material during repeated Na^+ intercalation/deintercalation cycles, thereby reinforcing the structural integrity and reducing mechanical stress, which further contributes to the long-term stability of the cathode. Therefore, CST-NFM exhibits an excellent capacity retention of 72.69% after 500 cycles, indicating superior long-term cycling stability compared to NFM. More importantly, the CST-NFM||HC full cell delivers an initial discharge specific capacity of 142.16 mAh g^{-1} and maintains a high capacity retention of 86.37% after 200 cycles, demonstrating great potential for practical commercial applications in SIBs. This work not only provides a feasible and scalable modification approach for designing high-performance, highly stable O3-type layered transition metal oxide cathodes but also reveals the intrinsic mechanism of inert ion co-doping in regulating oxygen redox activity and structural stability.

Author contributions

L. L. and K. L. proposed the concept and supervised the work; X. B. designed the experiments and wrote the paper; X. B., Q. Y., Y. W., M. L., G. Y., T. H. and X. Z. conducted the electrochemical measurements and analysed the resulting data; J. X. and T. L. helped summarize the data; L. L., K. L. and S. Z. helped summarize the data and supervised the research; All authors discussed the results and revised the manuscript. All authors have approved the final version of the manuscript.

Conflicts of interest

There are no conflicts to declare.

Data availability

The data supporting the findings of this study are available within the article or its supplementary information (SI). Supplementary information is available. See DOI: https://doi.org/10.1039/d6sc01429a.

Acknowledgements

This work was funded by the National Natural Science Foundation of China (22309002 and 52202286), China National Postdoctoral Program for Innovative Talents (BX20250118), Natural Science Foundation of Zhejiang Province (LY24B030006), Key Research and Development Program of Zhejiang Province (2024C01057), Natural Science Foundation of Hebei Province (E2024202239 and B2024202081), Science and Technology Plan Project of Wenzhou Municipality (ZG2024055), Science Research Project of Hebei Education Department (CXY2024036), and the Tianjin Science and Technology Plan Project (24JCQNJC00750). We would like to thank the Advanced Materials Testing and Analysis Center of the Hebei University of Technology. The authors extend their gratitude to Scientific Compass (https://www.shiyanjia.com/) for providing invaluable assistance for EPR.

Notes and references

1 C. Guo, X. Y. Fan, M. T. Liu, S. W. Xu, G. X. Wei, Z. B. Chen, Z. K. Guan, Y. Xiao, H. Xin and P. F. Wang, *Carbon Energy*, 2025, e70037.
2 H. Zhang, Y. Gao, X. H. Liu, L. F. Zhou, J. F. Li, Y. Xiao, J. Peng, J. Z. Wang and S. L. Chou, *Adv. Energy Mater.*, 2023, **13**, 2300149.
3 J. H. Zhang, Y. D. Wang, Y. Q. Kang, H. Du, T. D. Jia, J. H. Xu, Y. L. Huang, Y. Zhao, F. Y. Kang and B. H. Li, *Energy Mater. Adv.*, 2024, **5**, 0128.
4 E. Gabriel, C. R. Ma, K. Graff, A. Conrado, D. W. Hou and H. Xiong, *eScience*, 2023, **3**, 100139.
5 M. Hassan, Y. S. Zhao, Q. Liu, W. X. He, S. A. Riza, D. B. Mu, L. Li, R. J. Chen and F. Wu, *Carbon Neutralization*, 2025, **4**, e70000.
6 F. X. Ding, P. X. Ji, Z. Han, X. Y. Hou, Y. Yang, Z. L. Hu, Y. S. Niu, Y. Liu, J. Zhang, X. H. Rong, *et al.*, *Nat. Energy*, 2024, **9**, 1529–1539.
7 Y. J. Guo, R. X. Jin, M. Fan, W. P. Wang, S. Xin, L. J. Wan and Y. G. Guo, *Chem. Soc. Rev.*, 2024, **53**, 7828–7874.
8 L. Yang, R. S. Chen, Z. P. Liu, Y. R. Gao, X. F. Wang, Z. X. Wang and L. Q. Chen, *Battery Energy*, 2022, **1**, 20210015.
9 C. Delmas, D. Carlier and M. Guignard, *Adv. Energy Mater.*, 2021, **11**, 2001201.
10 Z. G. Chen, Y. Y. Deng, J. Kong, W. B. Fu, C. Y. Liu, T. Jin and L. F. Jiao, *Adv. Mater.*, 2024, **36**, 2402008.
11 D. S. Fan, Q. Y. Shen, H. Li, X. H. Qu, L. F. Jiao and Y. C. Liu, *Energy Mater. Adv.*, 2024, **5**, 0073.
12 Y. L. Huo, H. Guo, Z. Z. Hong, L. Xie, Y. C. He, W. N. Cao, M. W. Xu, Y. Xiao and Y. R. Qi, *Angew. Chem., Int. Ed.*, 2025, **64**, e202513023.
13 X. H. Liang, J. Y. Hwang and Y. K. Sun, *Adv. Energy Mater.*, 2023, **13**, 2301975.
14 Z. Lian, H. B. Wang, Z. Chen, C. L. Xu, H. Yu, F. X. Ding, H. C. Mao, D. Yu, Y. Yang, B. W. Wang, *et al.*, *ACS Energy Lett.*, 2025, **10**, 1517–1528.
15 W. D. Xu, C. Cheng, L. Wang, T. Chen, Z. Zhou, T. R. Yan, S. Q. Shen, P. Zeng and L. Zhang, *Adv. Energy Mater.*, 2026, **16**, e04557.

16 C. Guhl, J. Rohrer, P. Kehne, T. Ferber, L. Alff, K. Albe, W. Jaegermann, P. Komissinskiy and R. Hausbrand, *Energy Storage Mater.*, 2021, **37**, 190–198.
17 E. Y. Hu, X. Q. Yu, R. Q. Lin, X. X. Bi, J. Lu, S. Bak, K. W. Nam, H. L. Xin, C. Jaye, D. A. Fischer, *et al.*, *Nat. Energy*, 2018, **3**, 690–698.
18 W. Y. Huang, J. M. Qiu, Z. Q. Zhuo, J. G. Wen, Y. Q. Guo, Y. F. Yuan, Z. F. Chen, J. T. Hu, T. Y. Li, L. R. Zheng, *et al.*, *J. Am. Chem. Soc.*, 2025, **147**, 26218–26225.
19 H. J. Dong, H. L. Liu, Y. J. Guo, Y. H. Feng, X. Zhu, S. W. Xu, F. X. Sui, L. Z. Yu, M. T. Liu, J. Z. Guo, *et al.*, *J. Am. Chem. Soc.*, 2024, **146**, 22335–22347.
20 S. Kim, J. A. Lee, D. G. Lee, J. Son, T. H. Bae, T. K. Lee and N. S. Choi, *ACS Energy Lett.*, 2024, **9**, 262–270.
21 J. N. Huang, Z. C. Xue, S. J. Lee, H. Y. Chen, X. B. Ji and K. Du, *J. Am. Chem. Soc.*, 2025, **147**, 22444–22452.
22 Y. Yu, D. Ning, Q. Y. Li, A. Franz, L. R. Zheng, N. Zhang, G. X. Ren, G. Schumacher and X. F. Liu, *Energy Storage Mater.*, 2021, **38**, 130–140.
23 A. Jiang, H. G. Xie, Q. L. Lin, Z. Xiao, F. Wang, X. M. Zhang, W. W. Zhang, W. He, Z. F. Qian, X. Y. Dai, *et al.*, *Adv. Funct. Mater.*, 2026, **36**, e19006.
24 S. Huang, Y. Y. Sun, T. Yuan, H. Y. Che, Q. F. Zheng, Y. X. Zhang, P. Z. Li, J. Qiu, Y. P. Pang, J. H. Yang, *et al.*, *Carbon Neutralization*, 2024, **3**, 584–596.
25 N. Y. Hong, J. W. Li, H. J. Wang, X. Y. Hu, B. Zhao, F. Hua, Y. Mei, J. N. Huang, B. C. Zhang, W. S. Jian, *et al.*, *Adv. Funct. Mater.*, 2024, **34**, 2402398.
26 Z. Y. Song, S. Kansara, S. S. Cheng, M. R. Yang, F. Li, C. H. Qi, S. Y. Li, J. Y. Hwang and Y. Bai, *ACS Energy Lett.*, 2025, **10**, 5199–5208.
27 J. Wu, W. B. Zhou, S. Zhang, J. H. Wang, J. Dong, C. X. Ma, K. Zhang, Y. Lu, Z. H. Yan, M. Z. Song, *et al.*, *Angew. Chem., Int. Ed.*, 2025, **64**, e202519551.
28 T. Zhang, Z. H. Song, Y. S. Li, Y. H. Huang, J. Y. Su, W. B. Hua and F. J. Li, *Angew. Chem., Int. Ed.*, 2025, **64**, e202509816.
29 K. Zhang, J. W. Zou, Z. M. Xu, G. P. Liu, L. H. He, Q. Yu, F. Wang and Y. Y. Xia, *J. Am. Chem. Soc.*, 2025, **147**, 48147–48157.
30 S. Shi, Q. Yang, S. M. Sui, S. Li, Y. Zhang, Z. Chen, Y. N. Wu, M. M. Fan, T. T. Huo, X. J. Bai, *et al.*, *Nano Lett.*, 2025, **36**, 10034–10043.
31 A. Joshi, S. Chakrabarty, S. H. Akella, A. Saha, A. Mukherjee, B. Schmerling, M. Ejgenberg, R. Sharma and M. Noked, *Adv. Mater.*, 2023, **36**, 2304440.
32 Z. Chen, Y. N. Wu, Q. Yang, T. T. Huang, S. Li, S. Shi, Y. Zhang, M. M. Fan, T. T. Huo, X. J. Bai, *et al.*, *Nano Res.*, 2024, **18**, 94907607.
33 Y. C. Huang, S. Gu, X. Xu, Z. B. An, X. D. Han, Y. L. Cao, D. S. He, F. C. Zhang, H. Guo, Y. Liu, *et al.*, *Adv. Mater.*, 2025, **37**, 2408012.
34 N. H. Xu, Y. J. Li, H. Y. Hu, G. Y. Zhang, S. Q. Su, H. Y. Dai, Y. F. Zhu, L. P. Zhang, Y. Yu and Y. Xiao, *Adv. Funct. Mater.*, 2026, e31271.
35 N. Ahmad, L. Yu, M. U. Muzaffar, B. Peng, Z. Z. Tao, S. Khan, A. Rahman, J. C. Liang, Z. X. Jiang, X. Y. Ma, *et al.*, *Adv. Energy Mater.*, 2025, **15**, 2404093.
36 L. W. Dong, W. Wu, Z. M. Xu, Y. H. Xiang, Z. Z. Liu, Y. Q. Jiang, Z. H. Liu, R. Monteiro, L. Parreira, H. Dou, *et al.*, *J. Power Sources*, 2025, **640**, 236701.
37 W. B. Lai, F. Q. Luo, L. X. Zeng, Z. Y. Lai, K. Jia, F. Y. Xiao, L. H. Chen, Y. Lu, Q. R. Qian, Q. H. Chen, *et al.*, *Adv. Funct. Mater.*, 2025, **36**, e17602.
38 Q. N. Zhou, Y. Li, S. Q. Li, Z. L. Wang, Q. J. Li, X. Y. Lu, Z. X. Qiu, C. Wu and Y. Bai, *Adv. Funct. Mater.*, 2025, **35**, e09825.
39 S. N. Gao, Y. H. Huang, J. R. Geng, W. Hu, K. Feng, J. Zhong, C. H. Yu and F. J. Li, *ACS Energy Lett.*, 2025, **10**, 4140–4147.
40 J. L. Kuang, Z. M. Liu, L. Fu, Y. Shi, M. J. Zhang, Y. Wang, N. Ding, D. Sun, Y. G. Tang and H. Y. Wang, *Angew. Chem., Int. Ed.*, 2025, **64**, e202500715.
41 Z. X. Huang, T. Q. Yang, J. M. Cao, K. Y. Zhang, Y. Liu, B. J. Xin, K. Xu, Y. Liu, X. Y. Zhou, J. Z. Guo, *et al.*, *Angew. Chem., Int. Ed.*, 2025, **64**, e202505367.
42 X. B. Jia, Q. Q. Peng, Y. F. Liu, D. C. Chen, J. Q. Wang, J. Y. Li, Y. F. Zhu, N. H. Xu, L. Y. Kong, H. X. Liu, *et al.*, *Nat. Commun.*, 2025, **16**, 10477.
43 H. B. Wang, H. Tang, T. Lin, H. Yu, X. Liu, J. Zhang, H. Guo, S. Y. Xia, B. J. Zhang, X. B. Zhao, *et al.*, *ACS Energy Lett.*, 2026, **11**, 537–547.
44 Y. Y. Deng, T. Jin, C. Li, T. Zhang, W. j. Zhang, S. J. Cui, C. Shen, L. F. Jiao, H. T. Huang and K. Y. Xie, *Energy Storage Mater.*, 2025, **74**, 103935.
45 S. N. Gao, Z. Zhu, H. Y. Fang, K. Feng, J. Zhong, M. C. Hou, Y. H. Guo, F. Li, W. Zhang, Z. F. Ma, *et al.*, *Adv. Mater.*, 2024, **36**, 2311523.
46 Q. Wang, G. H. Yu, B. Luo, W. J. Ji, Z. H. Liu, M. H. Li, Y. T. Nong, Y. Tian, X. W. Wang, J. F. Zhang, *et al.*, *ACS Nano*, 2024, **18**, 18622–18634.
47 C. Cheng, Y. H. Shen, C. Chen, S. M. Tang, Z. Q. Zhuo, Q. J. Niu, C. Yuan, T. Chen, L. Wang, J. H. Guo, *et al.*, *Adv. Energy Mater.*, 2025, **15**, e04261.
48 K. Fang, J. H. Yin, G. F. Zeng, Z. X. Wu, Y. L. Tang, D. Y. Yu, H. Y. Luo, Q. R. Liu, Q. H. Zhang, T. Qiu, *et al.*, *J. Am. Chem. Soc.*, 2024, **146**, 31860–31872.
49 W. Li, Z. Li, L. Li, A. J. Merryweather, Y. Chen, S. Yang, H. Shi, Y. Lu, Y. Qiu, G. Tan, *et al.*, *Energy Environ. Sci.*, 2025, **18**, 6032–6042.
50 A. Toumar, S. Ong, W. Richards, S. Dacek and G. Ceder, *Phys. Rev. Appl.*, 2015, **4**, 064002.
51 F. X. Ding, C. L. Zhao, D. D. Xiao, X. H. Rong, H. B. Wang, Y. Q. Li, Y. Yang, Y. X. Lu and Y. S. Hu, *J. Am. Chem. Soc.*, 2022, **144**, 8286–8295.
52 Y. F. Li, Q. Fang, Y. C. Zheng, L. W. Fan, Y. Sun, X. F. Wang and H. L. Pan, *Adv. Energy Mater.*, 2026, **16**, e06239.
53 T. F. Song, L. Chen, D. Gastol, B. Dong, J. F. Marco, F. Berry, P. Slater, D. Reed and E. Kendrick, *Chem. Mater.*, 2022, **34**, 4153–4165.
54 X. Gao, J. Chen, H. Q. Liu, S. Y. Yin, Y. Tian, X. Y. Cao, G. Q. Zou, H. S. Hou, W. F. Wei, L. B. Chen, *et al.*, *Chem. Eng. J.*, 2021, **406**, 126830.
55 Q. J. Mao, J. C. Zhang, D. Wong, W. Yin, R. Y. Wang, T. R. Zhang and X. F. Liu, *Angew. Chem., Int. Ed.*, 2024, **63**, e202404330.

56 R. Y. Liu, S. J. Yang, S. T. Zhou, J. X. Xing, X. W. Niu, G. Y. Pang, G. C. Liu, F. Ye, B. W. Xiao and C. Xu, *Small*, 2025, **21**, e05197.
57 K. Zhang, Z. M. Xu, G. D. Li, R. J. Luo, C. Ma, Y. G. Wang, Y. N. Zhou and Y. Y. Xia, *Adv. Energy Mater.*, 2023, **13**, 2302793.
58 Y. Mao, H. C. Gong, X. Y. Wang, Y. Cao, S. W. Wang, K. Ma, X. G. Fuku, C. Y. Zhou and J. Sun, *Adv. Energy Mater.*, 2025, **15**, 2502592.
59 T. W. Cui, L. X. Liu, Y. X. Xiang, C. C. Sheng, X. Li and Y. Z. Fu, *J. Am. Chem. Soc.*, 2024, **146**, 13924–13933.
60 Y. S. Niu, Z. L. Hu, B. Zhang, D. D. Xiao, H. C. Mao, L. Zhou, F. X. Ding, Y. Liu, Y. Yang, J. P. Xu, *et al.*, *Adv. Energy Mater.*, 2023, **13**, 2300746.
61 C. Y. Jiang, Y. S. Wang, Y. H. Xin, Q. B. Zhou, Y. F. Pang, B. R. Chen, Z. Y. Wang and H. C. Gao, *J. Mater. Chem. A*, 2024, **12**, 13915–13924.
62 Y. Y. Xie, H. Wang, G. L. Xu, J. J. Wang, H. P. Sheng, Z. H. Chen, Y. Ren, C. J. Sun, J. G. Wen, J. Wang, *et al.*, *Adv. Energy Mater.*, 2016, **6**, 1601306.
63 L. Y. Kong, J. Y. Li, H. X. Liu, Y. F. Zhu, J. Q. Wang, Y. F. Liu, X. Y. Zhang, H. Y. Hu, H. H. Dong, Z. C. Jian, *et al.*, *J. Am. Chem. Soc.*, 2024, **146**, 32317–32332.
64 L. Q. Mu, X. Feng, R. H. Kou, Y. Zhang, H. Guo, C. X. Tian, C. J. Sun, X. W. Du, D. Nordlund, H. L. Xin, *et al.*, *Adv. Energy Mater.*, 2018, **8**, 1801975.
65 Y. Wang, X. D. Zhao, J. T. Jin, Q. Y. Shen, Y. Hu, X. B. Song, H. Li, X. H. Qu, L. F. Jiao and Y. C. Liu, *J. Am. Chem. Soc.*, 2023, **145**, 22708–22719.
66 L. B. Yao, P. C. Zou, C. Y. Wang, J. H. Jiang, L. Ma, S. Tan, K. A. Beyer, F. Xu, E. Y. Hu and H. L. Xin, *Adv. Energy Mater.*, 2022, **12**, 2201989.